Transmission imaging on a scintillator in a scanning electron microscope

Zuidema, Wilco; Kruit, Pieter

DOI
10.1016/j.ultramic.2020.113055

Publication date
2020

Document Version
Final published version

Published in
Ultramicroscopy

Ultramicroscopy 218 (2020) 113055

Contents lists available at ScienceDirect

Ultramicroscopy

journal homepage: www.elsevier.com/locate/ultramic

Transmission imaging on a scintillator in a scanning electron microscope

Wilco Zuidema*,[a], Pieter Kruit[a]

Delft University of Technology, Mekelweg 5, 2628CD, Delft, The Netherlands

A B S T R A C T

Large area electron microscopy (EM) imaging has long been difficult due to fundamental limits in throughput for conventional electron microscopes. New developments in transmission electron microscopy and multi-beam scanning electron microscopy (MBSEM) imaging have however made it possible to generate large EM datasets [1,2,3]. This article describes a transmission imaging technique that is suitable for a MBSEM as it allows for a relatively straightforward way of separating the signals generated by each beam. The technique places a thin (50nm-200nm) tissue section directly on top of a coated scintillator. The electrons that are transmitted through the section generate light in the scintillator which is collected by a high NA objective and imaged onto a photon detector. This article gives a model for the contrast-to-noise (CNR) and signal-to-noise (SNR) ratio that is to be expected for this imaging technique. These parameters were calculated using Monte-Carlo simulations. It was found that the CNR increases when decreasing landing energy and SNR increases with increasing landing energy. These two trends cause that there is an intermediate energy where imaging performance is best. The energy of this optimum was calculated for various levels of heavy metal staining, section thickness, coating material, coating thickness and light collection efficiency. The model was verified experimentally on a synthetic sample.

1. Introduction

In the last decade, there has been a major push for large volume scanning electron microscopy, of which the most striking example is full brain connectomics [4,5]. This development was made possible by the ability to store the large datasets involved, as well as by the increasing work being done on automatic segmentation of this data [6–9]. The throughput speed in SEM imaging is limited by the maximum probe current allowable to obtain a desired resolution. This limitation can be circumvented by employing multiple beams in one SEM. In these Multi-Beam SEM's (MBSEM) the maximum throughput is governed primarily by the number of beams and detector bandwidth. The current per beam is still limited but the theoretical throughput speed scales linearly with the number of beams. The ZEISS MultiSEM already has been available for some time, which has up to 91 beams (up to 331 beam proven [10]) with secondary electron (SE) detection [2,3]. Delft University of Technology has, over the past decade, developed a MBSEM with 196 beams [11].

Signal detection in the MBSEM with regular detectors is impossible. In such microscopes the signal generated by each beam has to be physically separated. In the ZEISS MultiSEM this is performed by focusing the secondary electrons from the sample, through a separate optical system, onto a detector array. In our MBSEM, with 64 beams, we employ a transmission imaging technique which makes for a relatively straightforward separation of the signals created by the multiple beams [12]. This circumvents the need for extra electron optics and leaves the SEM column unchanged. The imaging is performed with a low energy electron beam (2-10keV) similar to methods using a solid state detector [13,14] or an SE based transmission detector [15]. In our method we place the tissue section directly on top of a thin scintillator screen (thinner than 200μm) which is coated with a conductive layer. The light signal generated by the electrons transmitted through the sample is collected by a high NA objective lens and the light is imaged onto a photon detector outside of the vacuum chamber. Alternatively, the detector could be placed in vacuum, directly underneath the scintillator. An overview of the detection method is shown in Fig. 2. This method was first developed by A. Boyde [16], who placed a thick section on top of a glass substrate and collected the cathodoluminescence created by the transmitted electrons. By using a scintillator instead of glass, the light output and thus the DQE is greatly increased and the use of an ultrathin section gives a higher image resolution than a thick section. Compared to other detection methods, the collection efficiency of the detection is very high and is only limited by the backscatter coefficient of the scintillator. It has been shown that this imaging method can be used to image, heavy metal stained and embedded biological tissue sections [12]. Results of tissue imaging are shown in Fig. 1, where the transmission imaging is compared to backscatter imaging. The sample is a 70nm thick section of rat pancreas, prepared according to the OTO protocol and embedded in EPON. Fig. 1a and 1b show, at first glance, a large similarity in both contrast and signal-to-noise ratio (SNR) for both imaging modalities. Fig. 1c and 1d show that in some cases, the transmission imaging can give contrast in locations where there is hardly any in backscatter imaging (highlighted by the arrow). In previously published work we have already

* Corresponding author.
E-mail address: w.zuidema@tudelft.nl (W. Zuidema).

https://doi.org/10.1016/j.ultramic.2020.113055
Received 10 February 2020; Received in revised form 15 June 2020; Accepted 21 June 2020
Available online 02 July 2020

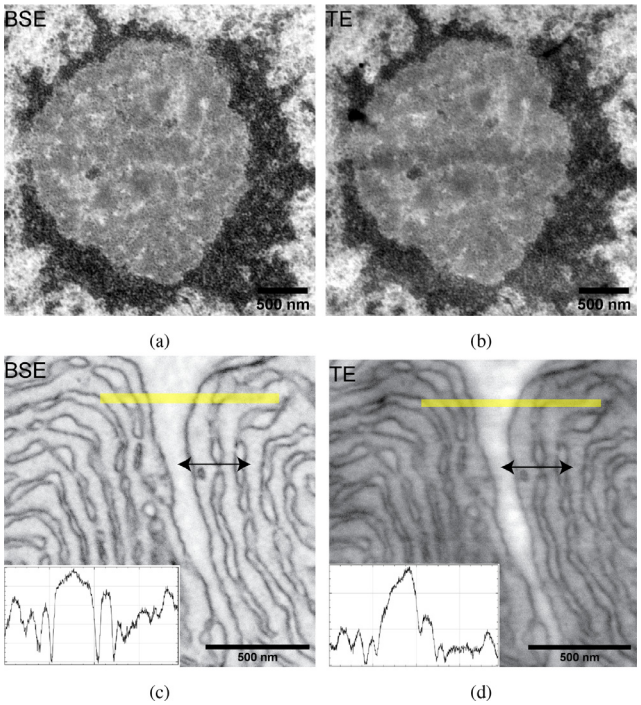

Fig. 1. SEM image of a nucleolus (a,b) and endoplasmic recticulum and cytoplasm (c,d) in rat pancreas, (a,c) (inverted) backscatter compared to (b,d) transmission imaging.Images a,b acquired with a landing energy of 4keV, c,d were acquired at 3.5keV. All images were stretched to full dynamic range and acquired at a 16 bit pixel depth. (a,b) show similar contrast where the images (c,d) show that the contrast in transmission imaging can be greatly different from backscatter imaging, as indicated by the arrow. This is illustrated by the line profile taken along the yellow line (inset in figure c and d). The peak in the line profile is much higher in the case of transmission imaging.

drawn some conclusions about the image quality using a semi-analytical method [17]. This paper is dedicated to analyzing the quality of the detection method and determine the optimum imaging conditions. This is done with a more rigorous Monte Carlo simulation method to aid some over simplifications from the previous work. The outcome is then compared to backscatter detection.

2. Monte Carlo model

2.1. Performance parameters

In order to evaluate the optical transmission detection system and to compare it to backscatter imaging, two parameters are considered. These parameters are Contrast-To-Noise Ratio (CNR) and SNR. The most well known parameters of these two is SNR. In this article the SNR which is referred to is the detected SNR at the end of the detection chain (SNR_{out}). The CNR and SNR are given by Eqs. (2.1) and (2.2).

$$CNR = \frac{\mu_{1out} - \mu_{2out}}{\sqrt{\sigma_{1out}^2 + \sigma_{2out}^2}} \tag{2.1}$$

$$SNR_1 = \frac{\mu_{1out}}{\sigma_{1out}} \qquad SNR_2 = \frac{\mu_{2out}}{\sigma_{2out}} \tag{2.2}$$

The CNR gives a quantification of how well two features are contrasted against the noise on those features. μ_1 and μ_2 are the expectation values of the signal of the two features, in our case the amount of detected transmitted or backscattered electrons and σ_1 and σ_2 are the standard deviations of these signals. An example in a simulated image of the effect of SNR and CNR is shown in Fig. 3. The image shows two lines with lower transmission coefficient than the background. The CNR is calculated between the background and the lines. The SNR is the

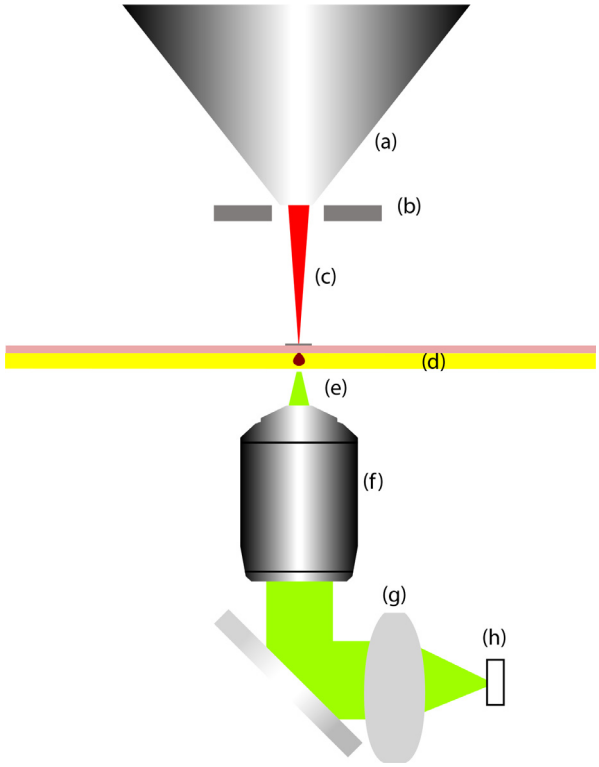

Fig. 2. An overview of the detection method as described. (a) The SEM polepiece, (b) backscatter detector, (c) electron beam, (d) ultrathin tissue section on a conductive coating on a scintillator, (e) scintillation light, (f) high NA light microscope objective, (g) light imaging system (can consist of multiple lenses and windows), (h) photon detector.

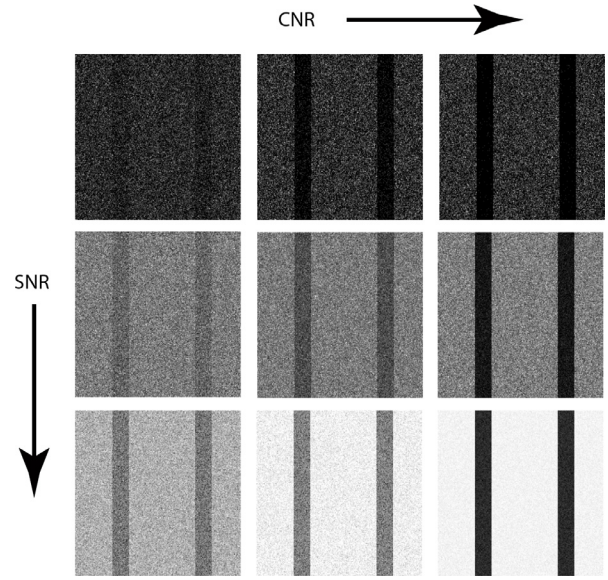

Fig. 3. From left to right showing the effect of increasing CNR and/or SNR. The image was simulated for transmission imaging with binomial noise. It shows that if there is a high SNR and a high CNR image quality can be considered best.

average SNR over the whole image. The images were stretched to full dynamic range, which means maximum digital contrast without clipping. It shows that just a high SNR or CNR will not give a good image. When we consider a low SNR and CNR, the lines are hardly visible. Low SNR but high CNR has very clearly defined lines. But even if the CNR is low, and the SNR is high, still the lines are visible. The best looking image is however that in which both the SNR and CNR are high [18].

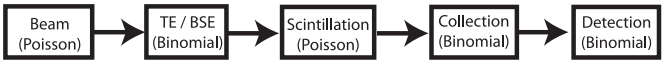

Fig. 4. The cascading noise model used for the SNR and CNR calculations.

To calculate the SNR and CNR in a final image, the whole detection system has to be taken into account. For this analysis a cascading noise model is used as developed by F. Timischl [18,19]. The cascade of noise here is as follows. In the imaging system there are five conversion steps which add noise to the eventual signal (see Fig. 4). The first of which is the shot noise on the primary electron beam, which follows Poisson statistics. The second is the generation of the transmission or backscattered electrons in the sample, which follow binomial statistics. The third stage is scintillation, which follows Poisson statistics. The last two stages are the collection of the light by the objective lens and the detection, which follow binomial statistics. The detector with typically a total gain of 10^6 was omitted as it adds no noise by itself. Readout noise and detector dark noise are left out of the calculation, as both are considered to be avoidable. The scintillation is, in this work, omitted for backscatter imaging, as various detector setups are possible [20] and the calculation is done for a best case scenario. The signal and the noise, μ_{1out}, μ_{2out}, σ_{1out}, σ_{2out} from Eq. (2.2) are calculated as shown in Eqs. (2.3) and (2.4).

$$\mu_{1out} = \mu_{1b}\mu_{1t}\mu_{1s}\mu_c\mu_d \tag{2.3a}$$

$$\mu_{2out} = \mu_{2b}\mu_{2t}\mu_{2s}\mu_c\mu_d \tag{2.3b}$$

$$\sigma_{1out} = \mu_{1out} \times \left(\frac{\sigma_{1b}^2}{\mu_{1b}^2} + \frac{\sigma_{1t}^2}{\mu_{1b}\mu_{1t}^2} + \frac{\sigma_{1s}^2}{\mu_{1b}\mu_{1t}\mu_{1s}^2} + \frac{\sigma_c^2}{\mu_{1b}\mu_{1t}\mu_{1s}\mu_c^2} + \frac{\sigma_d^2}{\mu_{1b}\mu_{1t}\mu_{1s}\mu_c\mu_d^2}\right)^{\frac{1}{2}} \tag{2.4a}$$

$$\sigma_{2out} = \mu_{2out} \times \left(\frac{\sigma_{2b}^2}{\mu_{2b}^2} + \frac{\sigma_{2t}^2}{\mu_{2b}\mu_{2t}^2} + \frac{\sigma_{2s}^2}{\mu_{2b}\mu_{2t}\mu_{2s}^2} + \frac{\sigma_c^2}{\mu_{2b}\mu_{2t}\mu_{2s}\mu_c^2} + \frac{\sigma_d^2}{\mu_{2b}\mu_{2t}\mu_{2s}\mu_c\mu_d^2}\right)^{\frac{1}{2}} \tag{2.4b}$$

Where μ_b, μ_t, μ_s, μ_c and σ_d are the expectation value and σ_b, σ_t, σ_s, σ_c and σ_d are the standard deviation of the beam, transmitted electrons (or backscattered), scintillation, light collection and the detector efficiency, respectively. Note that due to the scintillator term, which contains the deposited energy, the CNR is influenced by the energy loss in the sample. The number in the subscript is the area for which the number holds. For example, in this article, 1 would be resin and 2 would be a cell membrane. As shown by Timischl [18], the CNR is independent of contrast and brightness settings, where the SNR is not.

2.2. Monte Carlo model setup

To obtain the parameters in Eq. (2.2) which are needed for CNR and SNR calculation, Monte Carlo simulations were performed using the Casino simulation software [21]. The model used for this work is based on the imaging of Osmium fixed (stained) tissue embedded in an epoxy resin. In electron microscopy of tissue samples, most commonly Osmium-Tetroxide is used as a post-fixative after aldehyde fixation. Osmium tetroxide reacts and binds with the unsaturated lipids present in the tissue material, for instance cell membranes [22]. Furthermore, Osmium is a high atomic number, dense metal, which gives high contrast in all detection methods used in electron microscopy and is thus often seen as a stain as much as a fixative. It must be noted that, except for fixation and staining, the osmium present in the tissue also provides a conductive path for the electrons to the substrate, preventing charging. The amount of osmium at any place in the tissue is highly dependent on the composition of the tissue before fixation and numbers in literature vary greatly (from 2wt% to 15wt% [23–26]). For this model we will assume that the contrast generated in the biological material is completely generated by the Osmium and the comparatively light and low density native elements give no contrast. The sample provided is built up as follows: An ultra thin tissue section (50-100 nm), a Boron coating (10nm-130nm) and a YAG:CE substrate. The two different areas of the sample are bare epon, the embedding medium, and an Osmium fixated cell membrane with either 1wt%, 5wt% or 10wt% of Osmium. The full compositions are listed in Table 1. In the simulations, the electron beam, impinges on one of the materials for an energy varied between 1keV and 10 keV. From the Monte Carlo simulation three parameters are obtained for each energy. Those parameters are: the backscatter coefficient, the amount of electrons absorbed in the scintillator and the average energy these electrons deposit. These numbers are then used to fill in Eqs. (2.2) to (2.4), for a certain current and dwell time.

Table 2.1
Table showing the compositions of the materials used in the Monte Carlo simulations, compositions are given in wt %.

Material	Density (g/cm^3)	H	C	O	Os
Epon	1.22	0.080	0.63	0.29	0
Membrane 5% stain	2.29	0.080	0.63	0.24	0.05
Membrane 1% stain	1.43	0.080	0.63	0.28	0.01
Membrane 10% stain	3.35	0.080	0.63	0.19	0.1
		Y	Al	O	
YAG	4.56	0.45	0.23	0.32	

An example of the full transmission detection chain will now be given. The tissue section has a thickness of 70 nm, 5% staining (see Table 1) on the membrane and the scintillator has a 70 nm B coating. The landing energy is chosen to be 5keV at a current of 1nA and a dwell time of 1 μs. This current and dwell time gives on average 6241 electrons (μ_b) with a standard deviation of 79 (σ_b) electrons. The average transmission coefficients are calculated using Monte-Carlo simulations. These are, for the membrane: 0.73 and for the bare resin: 0.90 (μ_t). The standard deviations of the transmitted electrons are 0.44 and 0.3 (σ_t), respectively, according to the binomial distribution ($\sqrt{\mu_t(1-\mu_t)}$). The average energy deposition of the electrons in the scintillator is also taken from the simulations. The electrons are now converted to light with an estimated efficiency of 20 photons per keV per electron [27], giving an average of 59 photons per electron for the membrane and 73 for the bare resin (μ_s). These have standard deviations of $\sqrt{73}$ and $\sqrt{59}$ respectively, according to the Poisson distribution. The next two terms in the chain are no longer material dependent. The collection efficiency of the imaging system can be considered fairly low due to the limited numerical aperture of the objective lens (0.95) and reflection losses of the rest of the imaging system. The collection efficiency of the photons in our system is calculated by assuming a homogeneous light source in the YAG:CE. An optical air objective with an NA of 0.95 will now collect approximately 18% of the light, the other lenses and mirrors lower μ_c to 0.05 with a standard deviation of 0.21(σ_c). The detector has a limited fill factor and quantum efficiency at the wavelength of the scintillation light. From the supplier data sheet we find that μ_d is approximately 0.4 with a standard deviation of 0.49 (σ_d). Filling these numbers into Eqs. (2.2) to (2.4) gives a value of 7.4 for the CNR and a value of 49 and 57 for the SNR on the membrane and resin, respectively. Backscatter detection is calculated in the same fashion for the steps that are still valid: electron beam, backscatter generation and collection efficiency (assumed to be 0.5). The average SNR for backscatter imaging in this case is 12, and a CNR of 2. All these calculations give a single point in, for instance, Fig. 5.

3. Monte Carlo simulation of the model sample

A result of the model is shown in Fig. 5. It shows the dependence of both CNR and SNR on the landing energy for a 100nm section and a 70nm boron coating layer on top the scintillator. First we only consider

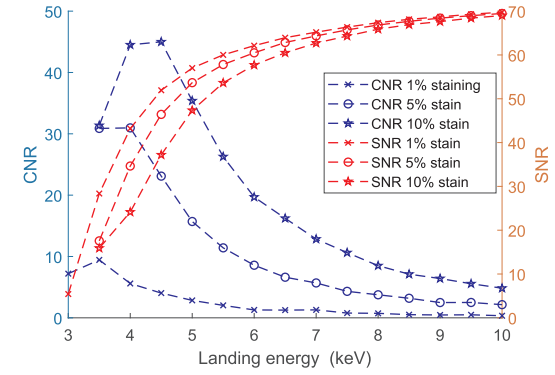

(a) .

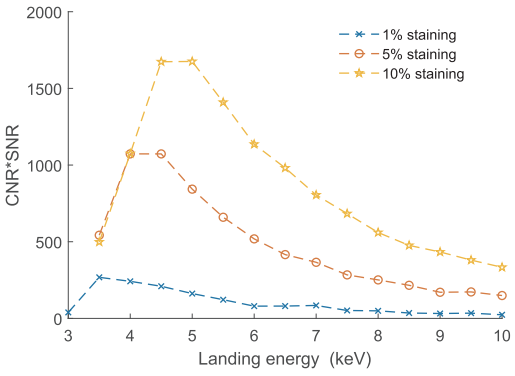

(b)

Fig. 5. Graphs showing the results of Monte Carlo Simulation, the effect of the level of staining on (a) the SNR and CNR and (b) the product of SNR and CNR. Staining improves the CNR significantly without reducing SNR.

the 5% staining case. The simulation was run from 1keV to 10keV but the graph starts at 3.5keV as below that energy, no electrons pass through the membrane anymore. Imaging here can still be performed but the contrast mechanism will be severely compromised and a CNR or SNR can no longer be calculated. Because of the difference in transmission coefficient between the membrane and the surrounding resin, the SNR values are slightly different for the two areas. In this graph the average of the two was taken, as in this model it is assumed that all other values lie in between the two extremes defined by the membrane and the resin. As the energy increases, more electrons pass through the tissue and create more photons in the scintillator, causing the SNR to rise with energy. At higher energy this is due to the generation of extra photons by each electron. On the other hand, the CNR drops with increasing energy until it almost reaches zero. This drop is caused by the difference in transmission coefficient between the membrane and the resin becoming smaller at higher energies. As the SNR and the CNR have opposite trends as a function of energy, an optimum energy will exist where both are high. There are different ways to define this optimum, in this article it will be assumed that the optimum lies where the product of SNR and CNR is maximized. At this maximum, the combination of the two has the highest possible value. For the case shown here this optimum lies at 4keV (5). The next question that arises from this result is, how does this optimum, and the levels of both SNR and CNR change with various levels of staining, coating thickness, scintillator yield and collection efficiency of the optical system.

Level of staining and section thickness

Depending on the application and specific tissue, the amount of staining can vary greatly. In order to investigate the effect of the level of staining, the content of osmium in the membrane is changes to 1wt% for low staining and 10 wt% for a high staining. The effect of the staining level in the transmission imaging is shown in Fig. 5. The staining level changes both the SNR and CNR levels, but clearly has the biggest effect on the CNR. The difference between the staining levels will severely effect the current and dwell time needed to get a good image. The optimum landing energy shifts to a higher energy as the amount of staining increases, from 3.5keV to 4.5keV. Here is where one should watch out, as when the wrong energy is chosen, the effect of extra staining can be undone. In general, the conclusion can be made that extra staining is always beneficial from a pure imaging perspective, as it will enhance the contrast without deteriorating the SNR greatly. There is no maximum to the amount of staining from an imaging perspective, as long as electrons can pass even the most densely stained areas of the sample.

Decreasing the section thickness from 100nm to 50nm has a similar effect as the change of staining level (figure omitted). This can be explained by the fact that the transmission of electrons through a material is mostly dependent on mass-thickness, the product of membrane thickness and its density [28]. This causes that changing the thickness and composition has a similar effect. The optimum imaging energy changes from 4 to 3.5keV, with the change in thickness as described. Increasing the section thickness will however result in a bad blurred membrane edges, as the membranes do not go straight down through the section but will in general always be at an angle.

Scintillator coating thickness and material

Because the scintillator is non-conductive, a conductive coating has to be applied to its surface to avoid charging. The coating material and thickness chosen for the previous analysis was 70nm of Boron. Boron was chosen because of it's low atomic number and density, causing a low absorption and backscatter coefficient. The thickness of 70nm was experimentally found to be the optimum as it allows for the electron beam to spread out significantly before hitting the scintillator. This ensures that the image is not contaminated with small scale imperfections in the scintillator or its surface. For reasons with the same considerations, it might be that a different coating thickness or material is preferred. First we analyze the effect of a different thickness of boron. The results of the calculation are shown in Fig. 6a, for a 5% stained section of 100nm thickness. As is to be expected, all the trends in SNR and CNR observed before are the same and independent of coating thickness. An interesting observation is that the variation in coating thickness does not so much change the levels of SNR and CNR but shifts them in energy. This is due to the coating layer acting as an amplifier for the difference in transmission coefficient between the two regions. This effect can also be seen in Fig. 6b, which shows a shift in the optimum energy for imaging.

A change of the material was also investigated and the result is shown in Fig. 7. For the change of material the mass density was kept constant to that of 70nm of B. This translates to a 54 nm Al layer and 16 nm Mo layer. From the graph it is clear that the imaging performance is dependent on the mass thickness of the coating and not so much on the material. There is however a chance that the imaging is influenced by imperfections in the coating layer, as the electron beam has less distance to be able to spread out, before hitting the scintillator surface. If Boron is not available, any other (conductive) metal can be used as long as the mass thickness is the same.

Detection parameters

Other efforts in the signal detection are the efficiency of the scintillator, the collection efficiency of the objective lens and the detection

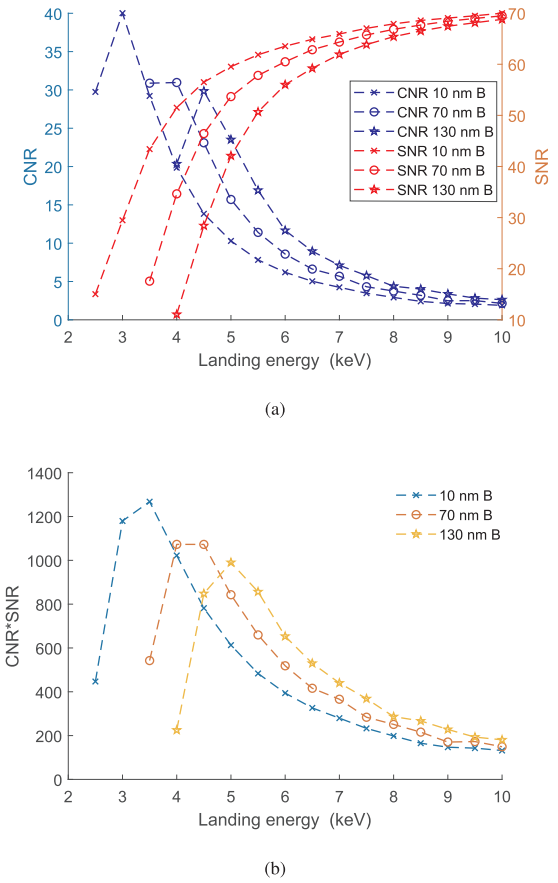

Fig. 6. Graphs showing the results of Monte Carlo Simulations, the effect of scintillator coating (Boron) thickness on (a) the SNR and CNR and (b) the product of SNR and CNR. The coating thickness shifts the optimal landing energy for imaging. The CNR is not affected, where the SNR is slightly reduced.

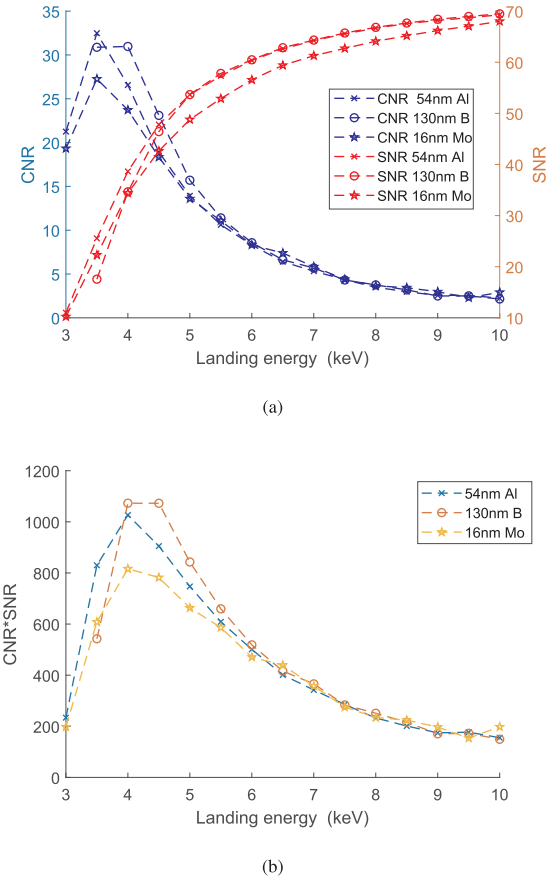

Fig. 7. Graphs showing the results of Monte Carlo Simulations, effect of the coating material, with a fixed mass-thickness, on (a) the SNR and CNR and (b) the product of SNR and CNR. The material that the coating is made of does not affect the imaging as long as the mass-thickness of the coating is the same.

efficiency of the detector. The collection efficiency of the objective lens can be increased by increasing the NA. Previous calculations were based on an air objective with an NA of 0.95. It has been shown that higher NA immersion objective up 1.4 can be used in vacuum [29], which gives a method to increase the collection efficiency. The effect of increased collection efficiency is shown in Fig. 8. Clearly an increase in collection efficiency would be beneficial for the detection system. A doubling of the collection efficiency, causes the both the SNR and the CNR to rise. The maximum product of these two parameters increases by a factor 1.5, when the collection efficiency is increased from 5% to 10%. Increasing the scintillator yield from 20 to 40 photons per keV per electron has the same effect as increasing the collection efficiency from 5 % to 20% (graph not shown).

Comparison to backscatter imaging

The most used imaging modality in SEM imaging of tissue is making use of the backscattered electrons. As the tissue section is flat and has hardly any topography, secondary electron imaging is generally less optimal. Backscatter imaging does not show the sample topography but the amount of staining in each position in the section. Areas with a higher density or atomic weight will show a higher backscatter signal, making for instance stained membranes visible. A free standing section and a section on a Kapton substrate were simulated for the calculations. For the calculation a Kapton substrate and a free standing section were simulated. Kapton was chosen because it is widely used in the atumtome serial sectioning system [30]. The free standing section is representative of a section on a TEM grid.

The result of simulations for a 5% stained membrane are shown in Fig. 9. As can be expected from expressions relating the backscatter coefficient to the landing energy [31], the backscatter coefficient for the free standing tissue increases with lower energy, increasing the SNR. For the tissue on kapton, the SNR is fairly constant, due to the background of the substrate on the backscatter electrons. This background however does not contain any information and the contrast does thus not change. The CNR gets slightly higher at higher energies, but does not change as much with energy as it does for transmission imaging. If backscatter imaging is compared to the transmission imaging, it stands out that both the CNR and SNR are lower for the 5% stain. The graph of the product of SNR and CNR was omitted in this comparison as the product in the case of backscatter imaging is too low to be reasonably compared to the transmission imaging case.

Comparison to secondary electron imaging.

In many studies secondary electron (SE) detection is used for imaging of heavy metal stained and resin embedded tissue sections [2,32–34]. Especially in MBSEM microscopes, SE's can be detected due to their relatively small energy spread. This spread allows for the focusing of the SE electron beams onto a detector [35,36]. The main disadvantage of this method of detection is that in general SE's are mostly generated by topographical features, of which there are non or few in the flat tissue sections. Therefore it is thought that the image formation contrast in the case of flat tissue samples is a result of so-called SE2 electrons, that is secondary electrons that are generated by backscattered electrons. This being an indirect process, extra noise is added in the SE generation step. Due to this, the images have less contrast and a lower signal to noise than TE and BSE imaging. A

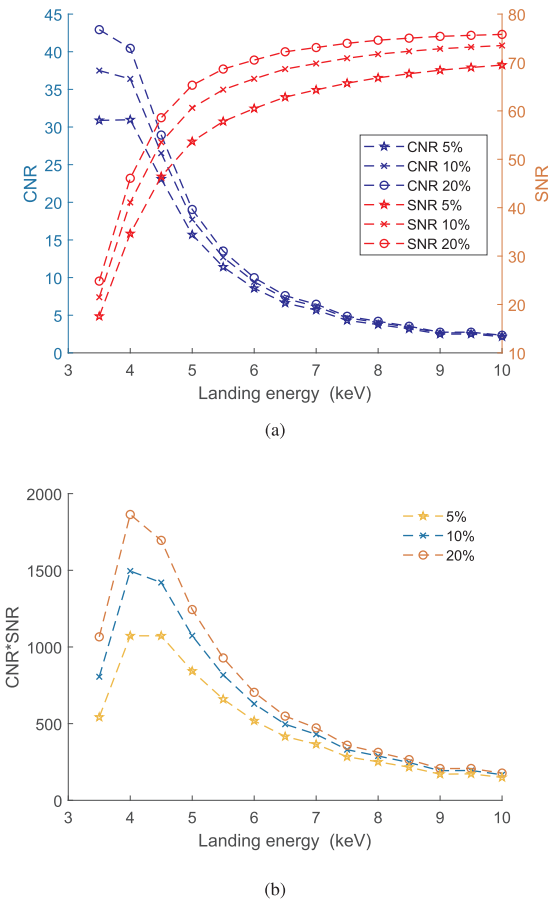

Fig. 8. Graphs showing the results of Monte Carlo Simulations, the effect of light objective collection efficiency on (a) the SNR and CNR and (b) the product of SNR and CNR. Increasing the light collection efficiency increases the SNR and SNR slightly.

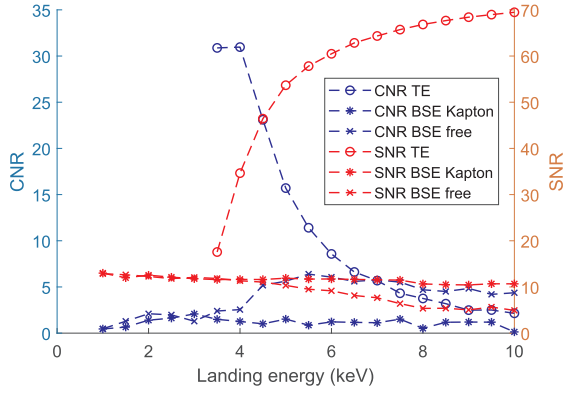

Fig. 9. Comparison between the CNR and SNR in transmission imaging (circles) and backscatter imaging (crosses). Both the CNR and SNR of transmission imaging are much higher in transmission imaging than backscatter imaging.

comparison is shown in Fig. 10. The image shown is that of OTO stained rat pancreas tissue embedded in EPON, with a 70nm section thickness. The SE image was taken at 2.5keV and the transmission image at 3keV, both with a 400pA beam current and a 800ns dwell time. The detector used for SE detection was an in-lens scintillation detector. The section showed charging effects at lower landing energies than 2.5keV. The TE image shows more contrast and a better SNR than the SE image.

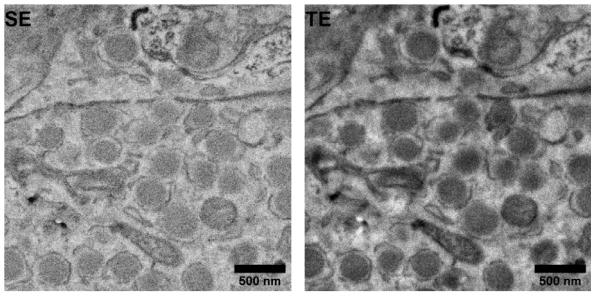

Fig. 10. OTO stained 70nm section of rat pancreas imaged at (a) 2.5keV landing energy with SE detection and at (b) 3keV landing energy with TE detection. Imaging was performed with a 400pA beam current and 800ns dwell time. Both image histograms have been stretched to full dynamic range. The TE image clearly shows more contrast and less noise than the SE image.

4. Experimental setup for model verification

The model as described in the previous section cannot be easily verified with fixated tissue sections. In a tissue section the exact composition at two different points is not known and the sample is extremely heterogeneous, so no two locations will have the same composition. Therefore another sample was manufactured: a YAG:CE scintillator substrate was half coated with 50nm Al and half with 50nm Cr. For these measurements a FEI Verios SEM was used, equipped with a Delmic SECOM integrated optical set-up [29]. SECOM is an integrated inverted fluorescent microscope, used for correlative light and electron microscopy. In this SECOM platform, the excitation path was removed and the system was only used for collecting the light generated in the scintillator. This light is collected using a 0.95 NA air objective, positioned directly underneath the scintillator, and focused on a Hamamatsu multi-pixel photon counter (s13360-3050sc). During the experiments the current was constant at 800pA and the dwell time was 5μs. The electron beam was defocused to a spot size of larger than 25μm to blur out all small scale defects that might be present in the Al or Cr layer. The low dwell time of 5μs was chosen in order to avoid possible bandwidth limitations in the detection path of the backscatter detector. Due to inhomogeneous light output of the scintillator, which is location dependent on scales larger than a few micrometers, the measurements were performed at random spots on the sample. To find the true SNR and to compensate for an offset (brightness) in the images, the measurements were done at 0.4nA and 0.8nA beam current and adjusted accordingly. At this current and dwell time, the amount of photons arriving at the detector within that dwell time is not lower than 2000. The dark count of the detector in that same time is 2, which can thus be neglected.

To check the model with actual tissue imaging, tissue from a rat pancreas was used. The tissue was prepared according to the OTO protocol [37] and cut to a 100nm section. The tissue was placed on top of a TEM grid which was then stuck to a Boron coated CRY18 scintillator with carbon tape. Because of the small space between the TEM grid and the scintillator, the beam can spread out after leaving the tissue, making sure that the image is not obscured by an inhomogeneous coating or scintillator defects. As mentioned before, it is hard to verify CNR results on tissue, but methods are available for estimating SNR in an SEM image. This method is described by Joy [38] and relies on the fact that if the pixel size in the image is taken small enough (much smaller than the size of the beam), two subsequent lines in the image are very similar and from those a SNR can be calculated by using the formula in Eq. (4.1), where X and Y are two successive lines in the image. This can now be done for all the lines in an image, giving an SNR. The pixel size was chosen to be 0.5nm, which is significantly smaller than the estimated probe size of about 4nm full-width half maximum. For every landing energy, three different images were taken

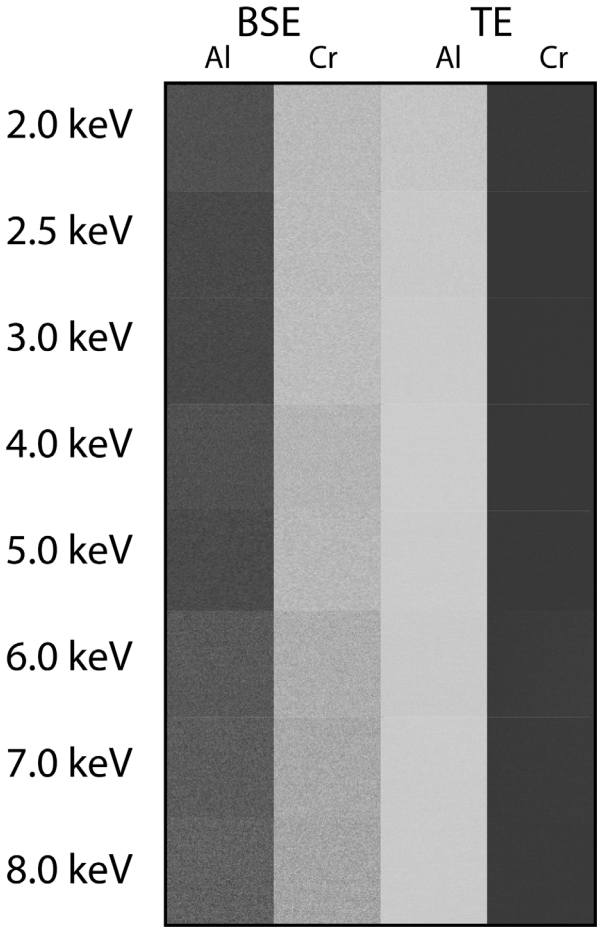

Fig. 11. Representation of experimental results to measure the CNR and SNR. The sample a scintillator half coated with 50nm Al and 50nm Cr. The example shown here are cutouts of the images used to find the CNR and SNR.

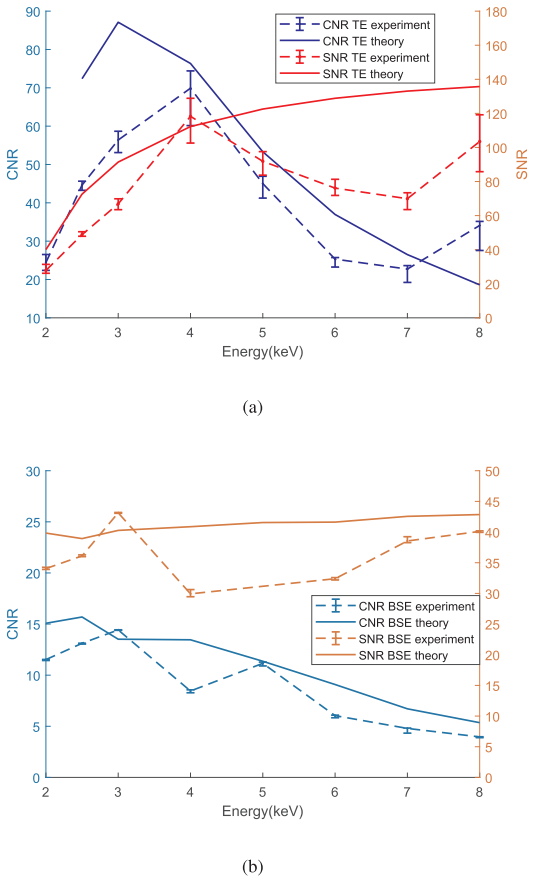

Fig. 12. Results of the SNR and CNR measurements on a sample with 50nm Cr and 50nm AL, for (a) transmission imaging and (b) backscatter imaging. The same trend and levels are observed in the model and the experiment.

and for those the SNR was calculated. Taking images of the same areas twice is not possible as imaging changes the sample, the transmission yield changes slightly and the sample tends to deform.

$$SNR = \frac{R_n}{1 - R_n} \text{ where } R_n = \frac{\text{cov}(X, Y)}{\sqrt{\text{var}(Y)\text{var}(Y)}} \tag{4.1}$$

5. Experimental results

A representation of the experimental results is shown in Fig. 11. It shows the two regions, Al and Cr in both backscatter and transmission. The image is scaled to full range and it shows that in TE imaging the contrast is higher than in BSE. Because Cr is a heavier metal than Al, we expect it to have lower transmission coefficient and a higher backscatter coefficient than Al, which we can immediately see in the image. In TE the noise is hardly visible due to the high contrast to noise ratio. This image clearly illustrates the better sensitivity to material density compared to backscatter imaging.

When analyzing the images we find the results shown in Fig. 12. Note that the average SNR is shown, as the SNR for the Cr and Al regions are different. First, inspecting the measured CNR and SNR for TE imaging, it shows that the expected trend is found. As the energy goes down, the CNR becomes larger, but at the same time fewer electrons reach the scintillator causing a drop in the SNR. At higher energy the opposite happens and the SNR rises and the CNR drops. Because of a lot of unknown factors in the measurement, namely objective lens collection efficiency, scintillator efficiency, small errors in the Monte Carlo simulation and precise thickness of the Cr and Al films, the absolute

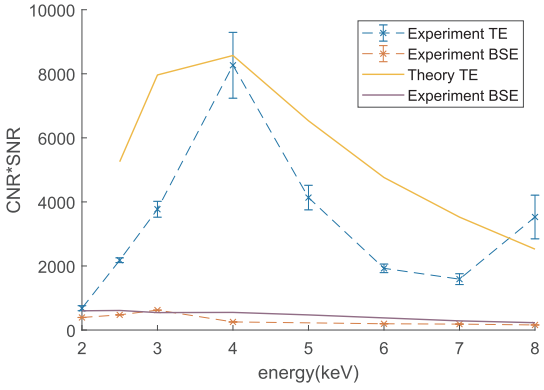

Fig. 13. The product of SNR and CNR for a 50nm Al and 50nm Cr layer as a function of landing energy. The same trend and levels are observed in the model and the experiment. The peak lies in the same location.

values were not compared with calculation results. The trends are however as expected. The product of SNR and CNR for the TE imaging, is shown in Fig. 13. The peak lies at the same position in the experiments as it does in calculations. As we have seen from the Monte Carlo model, collection efficiency and scintillator yield does not change the best energy for best imaging.

When comparing the transmission imaging to backscatter imaging, we have to keep in mind that the actual signal will be influenced by the

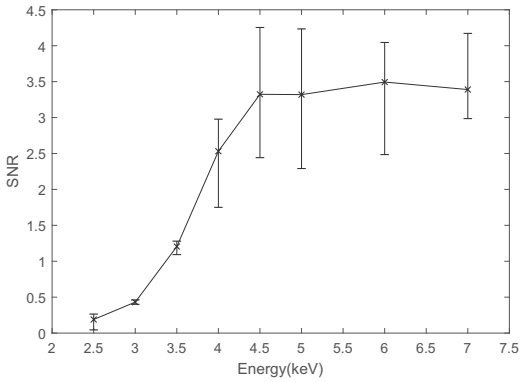

Fig. 14. Graph showing the measured (average) SNR as a function of landing energy for rat pancreas tissue. Measurements were done for with the same current and dwell time. It shows the decreasing SNR at low landing energy.

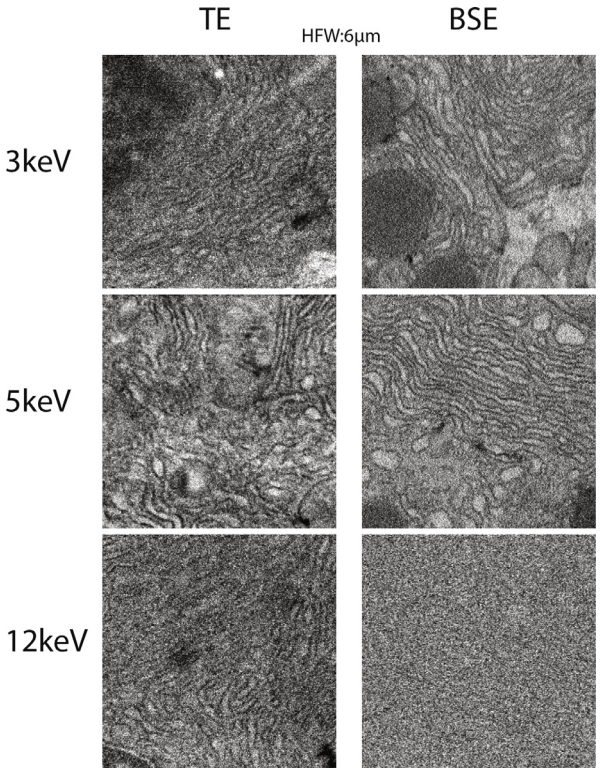

Fig. 15. Comparison of TE imaging and BSE imaging (inverted contrast) for landing energies of 3keV, 5keV and 12keV. The horizontal field width (HFW) is 6μm, a dwell time of 5μs and a beam current of 50pA.

scintillator substrate. The backscattered electrons from the scintilaltor will give an extra noise floor to the signal. The collection efficiency of the backscatter detector is an unknown, especially as this will be an energy dependent efficiency. Furthermore, we have not developed a full noise model of this detector. From Fig. 11 we can however see that the CNR in BSE imaging is much lower than for TE imaging. When looking at Fig. 12, it is clear that the levels for both CNR and SNR are much lower than in the TE imaging case.

The result from SNR measurements on tissue images is shown in Fig. 14. It can be seen here that the SNR increases with energy. After 7.5keV the calculation with Eq. (4.1) fails, as there is not enough detail in the image due to loss of contrast. Even though this method does not calculate the product of SNR and CNR, it is a convenient and quick way to find the optimum imaging energy, which is at the point where the SNR stops rising. Fig. 15 shows tissue images for three different landing energies compared for both TE and BSE imaging. At first glance the contrast and SNR look better in the TE images than they do in the BSE images. In the BSE case it is clear that the image quality goes up with lower energy, as the 3keV image seems to be the best. In TE imaging the difference is subtle but on close inspection it can be seen that the image is the best at 5keV. This is the same landing energy as was found from Fig. 14. The drop in CNR at higher energies is not very quick due to the fairly high staining in this tissue section.

6. Summary and conclusions

In summary, we have made a noise transfer model for transmission imaging in a MBSEM in order to calculate the CNR and SNR. The model considers the CNR between a stained membrane and the surrounding unstained embedding resin, in both transmission and backscatter imaging. The input variables for the model were calculated using Monte Carlo simulations. The model was verified using both a test sample and stained tissue sections. The effects of changing the staining, section thickness, scintillator coating material, thickness and detection parameters show that:

- There is a landing energy where the product of the CNR and SNR of the imaging method shows a maximum.
- Staining has an larger effect on the CNR than on the SNR. This also also holds for the section thickness. The CNR increases with increased staining and section thickness, where the SNR is fairly constant.
- The thickness of the Boron (or another material) coating on the scintillator shifts the optimum energy for imaging but has little effect on the imaging performance (SNR and CNR).
- Changing the scintillator coating material does not change the imaging performance if the mass-thickness is kept constant.
- Increasing the collection efficiency or scintillator quantum efficiency has a beneficial effect on the imaging performance, albeit relatively small compared to staining.
- The transmission imaging presented in this work performs better than backscatter imaging of heavy metal stained embedded tissue sections.

Concluding, the imaging method discussed in this paper can outperform backscatter imaging and is suitable for use in the MBSEM.

Declaration of competing interest

The authors declare that they have no known competing financial interests or personal relationships that could have appeared to influence the work reported in this paper.

Acknowledgments

The authors acknowledge Jacob Hoogenboom for advice on imaging and Ben Giepmans' group (University Medical Center Groningen) for biological tissue section preparation. This research was funded by FOM/NWO-i on FOM / FEl-programme 'The foundations for FASTER electron microscopy' (nr. i37).

References

[1] Z. Zheng, J.S. Lauritzen, E. Perlman, S. Saalfeld, R.D. Fetter, D.D. Bock, Z. Zheng, J.S. Lauritzen, E. Perlman, C.G. Robinson, M. Nichols, D. Milkie, B. Karsh, E.T. Trautman, J.A. Bogovic, P. Hanslovsky, G.S.X.E. Jefferis, M. Kazhdan, Resource A Complete Electron Microscopy Volume of the Brain of Adult Drosophila melanogaster A Complete Electron Microscopy Volume of the Brain of Adult Drosophila melanogaster, Cell (2018) 1–14, https://doi.org/10.1016/j.cell.2018.06.019.
[2] J.T. Neumann, T. Garbowski, W. Högele, T. Korb, S. Halder, P. Leray, R. Garreis,

M. le Maire, D. Zeidler, High-throughput multi-beam SEM: quantitative analysis of imaging capabilities at IMEC-N10 logic node, Metrology, Inspection, and Process Control for Microlithography XXXI 10145 (March 2017) (2017) 101451S, https://doi.org/10.1117/12.2257980.

[3] A.L. Eberle, S. Mikula, R. Schalek, J. Lichtman, M.L.K. Tate, D. Zeidler, High-resolution, high-throughput imaging with a multibeam scanning electron microscope, Journal of Microscopy 259 (2) (2015) 114–120, https://doi.org/10.1111/jmi.12224.

[4] K.L. Briggman, D.D. Bock, Volume electron microscopy for neuronal circuit reconstruction, Current Opinion in Neurobiology 22 (1) (2012) 154–161, https://doi.org/10.1016/j.conb.2011.10.022.

[5] N. Ohno, M. Katoh, Y. Saitoh, S. Saitoh, S. Ohno, Three-dimensional volume imaging with electron microscopy toward connectome, Microscopy (Oxford, England) 64 (1) (2015) 17–26, https://doi.org/10.1093/jmicro/dfu112.

[6] M. Joesch, D. Mankus, M. Yamagata, A. Shahbazi, R. Schalek, A. Suissa-Peleg, M. Meister, J.W. Lichtman, W.J. Scheirer, J.R. Sanes, Reconstruction of genetically identified neurons imaged by serial-section electron microscopy, eLife 5 (2016) 1–13, https://doi.org/10.7554/elife.15015.

[7] C. Sommer, C. Straehle, U. Kothe, F.A. Hamprecht, Ilastik: Interactive learning and segmentation toolkit, Proceedings - International Symposium on Biomedical Imaging (2011) 230–233, https://doi.org/10.1109/ISBI.2011.5872394.

[8] V. Kaynig, A. Vazquez-Reina, S. Knowles-Barley, M. Roberts, T.R. Jones, N. Kasthuri, E. Miller, J. Lichtman, H. Pfister, Large-scale automatic reconstruction of neuronal processes from electron microscopy images, Medical Image Analysis 22 (1) (2015) 77–88, https://doi.org/10.1016/j.media.2015.02.001.

[9] K. Lee, J. Zung, P. Li, V. Jain, H.S. Seung, Superhuman Accuracy on the SNEMI3D Connectomics Challenge (Nips, 1–11) (2017).

[10] C. Riedesel, I. Müller, N. Kaufmann, A. Adolf, N. Kaemmer, H. Fritz, A.L. Eberle, D. Zeidler, First demonstration of a 331-beam SEM, 1095931 (March) (2019) 114, https://doi.org/10.1117/12.2528795.

[11] C.W. Hagen, P. Kruit, C.W. Hagen, P. Kruit, Multibeam scanning electron microscope : Experimental results Multibeam scanning electron microscope : Experimental results, 5 (2010) (2016), https://doi.org/10.1116/1.3498749.

[12] Y. Ren, P. Kruit, Transmission electron imaging in the Delft multibeam scanning electron microscope 1 Transmission electron imaging in the Delft multibeam scanning electron microscope 1, Journal of Vacuum Science and Technology B 34 (2016), https://doi.org/10.1116/1.4966216.

[13] J. Kuipers, P. de Boer, B.N.G. Giepmans, Scanning EM of non-heavy metal stained biosamples: Large-field of view, high contrast and highly efficient immunolabeling, Experimental Cell Research 337 (2) (2015) 202–207, https://doi.org/10.1016/j.yexcr.2015.07.012.

[14] M. Kuwajima, J.M. Mendenhall, L.F. Lindsey, K.M. Harris, Automated Transmission-Mode Scanning Electron Microscopy (tSEM) for Large Volume Analysis at Nanoscale Resolution, PLoS ONE 8 (3) (2013) 1–14, https://doi.org/10.1371/journal.pone.0059573.

[15] U. Golla, B. Schindler, L. Reimer, Contrast in the transmission mode of a low-voltage scanning electron microscope, 173 (November 1993) (1994).

[16] S.R. A. Boyde, A new method of scanning electron microscopy for imaging biological tissues, Nature 302 (7) (1983) 522–523.

[17] W. Zuidema, J.P. Hoogenboom, P. Kruit, Improved Image Quality in SEM Imaging of Thin Tissue Sections, Microscopy and Microanalysis 23 (S1) (2017) 564–565, https://doi.org/10.1017/s1431927617003506.

[18] F. Timischl, The Contrast-to-Noise Ratio for Image Quality Evaluation in Scanning Electron Microscopy, SCANNING 37 (December 2014) (2015) 54–62, https://doi.org/10.1002/sca.21179.

[19] M.D.&S. F. Timischl, A Statistical Model of Signal Noise in Scanning Electron Microscopy, Scanning 3 (-) (2012) 137–144, https://doi.org/10.1002/sca.20282.

[20] J. Hejna, Noise coefficients ofbackscattered electron detectors for low voltage scanning electron microscopy, 252 (1) (2013) 35–48, https://doi.org/10.1111/jmi.12066.

[21] D. Drouin, A.R. Couture, D. Joly, X. Tastet, V. Aimez, R. Gauvin, CASINO V2.42 - A fast and easy-to-use modeling tool for scanning electron microscopy and microanalysis users, Scanning 29 (3) (2007) 92–101, https://doi.org/10.1002/sca.20000.

[22] H. Schatten, James Pawley, Biological Low-Voltage Scanning Electron Microscopy, 1, Springer Science, 2008, https://doi.org/10.1007/978-0-387-72972-5.

[23] K. Scott, N.W.M. Ritchie, Analysis of 3D elemental mapping artefacts in biological specimens using Monte Carlo simulation, Journal of Microscopy-Oxford 233 (October 2008) (2009) 331–339, https://doi.org/10.1111/j.1365-2818.2009.03124.x.

[24] P. Hennig, W. Denk, Point-spread functions for backscattered imaging in the scanning electron microscope, Journal of Applied Physics 102 (12) (2007), https://doi.org/10.1063/1.2817591.

[25] K.J. Hayworth, D. Peale, M. Januszewski, G.W. Knott, Z. Lu, C.S. Xu, H.F. Hess, GCIB-SEM : A path to 10 nm isotropic imaging of cubic millimeter volumes, im (2019).

[26] A.A. Sousa, A.A. Azari, G. Zhang, R.D. Leapman, Dual-axis electron tomography of biological specimens: Extending the limits of specimen thickness with bright-field STEM imaging, Journal of Structural Biology 174 (1) (2011) 107–114, https://doi.org/10.1016/j.jsb.2010.10.017.

[27] P. Schauer, J. Bok, Innovation possibilities of scintillation electron detector for SEM, IMC 2014, (2014).

[28] H.S. H DrescherL Reimer, Backscattering and secondary electron emission of 10-100 keV electrons in scanning electron microscopy, Z. ANGEW PHYSIK 29 (6) (1970).

[29] J.H.A.C Zonnevylle, R.F.C. van Tol, N. Liv, A.C. Narvaez, A.P.J. Effting., P. Kruit, Integration of a high-NA light microscope in a scanning electron, Journal of Microscopy 252 (1) (2013) 58–70, https://doi.org/10.1111/jmi.12071.

[30] D.G.C. Hildebrand, J.W. Lichtman, R.J. Weinberg, Imaging ATUM ultrathin section libraries with WaferMapper : a multi-scale approach to EM reconstruction of neural circuits, 8 (June) (2014) 1–18, https://doi.org/10.3389/fncir.2014.00068.

[31] L. Reimer, Scanning Electron Microscopy: Physics of Image Formation and Microanalysis, 2, Springer, 1998, https://doi.org/10.1007/978-3-540-38967-5.

[32] V. Le, M. Milani, F. Tatti, Focused ion beam (FIB)/scanning electron microscopy (SEM) in tissue structural research (2010) 41–48, doi:10.1007/s00709-010-0118-8.

[33] Y. Kubota, J. Sohn, Y. Kawaguchi, Large Volume Electron Microscopy and Neural Microcircuit Analysis, 12 (November) (2018) 1–12, https://doi.org/10.3389/fncir.2018.00098.

[34] Y. Kubota, J. Sohn, S. Hatada, M. Schurr, J. Straehle, A. Gour, R. Neujahr, T. Miki, S. Mikula, Y. Kawaguchi, A carbon nanotube tape for serial-section electron microscopy of brain ultrastructure, Nature Communications (2018) 1–3, https://doi.org/10.1038/s41467-017-02768-7.

[35] W. Ren, X. Liu, X. Hu, X. Luo, X. Ji, Q. Xi, W. Ren, X. Liu, X. Hu, X. Luo, X. Ji, Q. Xi, K. Chou, M. Ebert, E. Ma, inspection of wafer and mask (August 2019) (2020), doi:10.1117/12.2536565.

[36] Y. Ren, Imaging Systems for the Delft Multi- Beam Scanning Electron Microscope 1, (2017), https://doi.org/10.4233/uuid.

[37] A.M. Seligman, H.L. Wasserkrug, J.S. Hanker, A new staining method (oto) for enhancing contrast of lipid-containing membranes and droplets in osmium tetroxide-fixed tissue with osmiophilic thiocarbohydrazide (tch), The Journal of cell biology 30 (2) (1966) 424.

[38] D. Joy, SMART a program to measure SEM resolution and, Journal of Microscopy 2018 (Pt 1 October) (2002) 24–34, https://doi.org/10.1093/oxfordjournals.jmicro.a023869.